

# A Soft Robotic Morphing Wing for Unmanned Underwater Vehicles

Andrea Giordano, Liam Achenbach, Daniel Lenggenhager, Fabian Wiesemüller,\*  
Roger Vonbank, Claudio Mucignat, André Tristany Farinha, Pham Huy Nguyen,  
Robert Katzschmann, Sophie F Armanini, Ivan Lunati, Sukho Song, and Mirko Kovač\*

Actuators based on soft elastomers offer significant advantages to the field of robotics, providing greater adaptability, improving collision resilience, and enabling shape-morphing. Thus, soft fluidic actuators have seen an expansion in their fields of application. Closed-cycle hydraulic systems are pressure agnostic, enabling their deployment in extremely high-pressure conditions, such as deep-sea environments. However, soft actuators have not been widely adopted on unmanned underwater vehicle control surfaces for deep-sea exploration due to their unpredictable hydrodynamic behavior when camber-morphing is applied. This study presents the design and characterization of a soft wing and investigates its feasibility for integration into an underwater glider. It is found that the morphing wing enables the glider to adjust the lift-to-drag ratio to adapt to different flow conditions. At the operational angle of attack of  $12.5^\circ$ , the lift-to-drag ratio ranges from  $-70\%$  to  $+10\%$  compared to a rigid version. Furthermore, it reduces the need for internal moving parts and increases maneuverability. The findings lay the groundwork for the real-world deployment of soft robotic principles capable of outperforming existing rigid systems. With the herein-described methods, soft morphing capabilities can be enabled on other vehicles.

induced by variable buoyancy, into forward motion (see Section S1 and Figure S1, Supporting Information). Therefore, no active propulsion, such as propellers, is required. Wing efficiency, considered here as the lift-to-drag ratio, is a key parameter in enhancing the vehicle's performance. Unlike aircraft wings, underwater gliders' wings are required to invert the direction of the lift force to match that of the vehicle. Therefore, these wings feature symmetrical profiles to generate equal lift both in upward and downward gliding periods.<sup>[3]</sup> In order to reduce mechanical complexity, underwater gliders have no control surfaces, but at the cost of diminished maneuverability. Wings capable of changing shape (i.e., camber morphing) would be able to adapt to encountered gliding conditions. Therefore, their efficiency would be optimized and their operational range extended.<sup>[4]</sup> Additionally, independent operation of each wing would allow greater


maneuverability and control of the roll axis. Added advantages of such adaptive wings are enhanced resilience to collisions. An adaptive wing could also take advantage of various morphing principles, such as adjustable twist and airfoil camber.<sup>[5]</sup>

## 1. Introduction

Underwater gliders are a highly specialized type of vehicle.<sup>[1,2]</sup> They rely on winged locomotion, which converts vertical motion,

A. Giordano, L. Achenbach, D. Lenggenhager, F. Wiesemüller,  
A. Tristany Farinha, P. H. Nguyen, S. Song, M. Kovač  
Laboratory of Sustainability Robotics  
Empa - Swiss Federal Laboratories for Materials Science and Technology  
8600 Dübendorf, Switzerland  
E-mail: fabian.wiesemueller@empa.ch; mirko.kovac@empa.ch

A. Giordano, F. Wiesemüller, A. Tristany Farinha, P. H. Nguyen, S. Song,  
M. Kovač  
Aerial Robotics Laboratory  
Imperial College London  
South Kensington Campus, London SW7 2AZ, UK

 The ORCID identification number(s) for the author(s) of this article can be found under <https://doi.org/10.1002/aisy.202300702>.

© 2024 The Authors. Advanced Intelligent Systems published by Wiley-VCH GmbH. This is an open access article under the terms of the Creative Commons Attribution License, which permits use, distribution and reproduction in any medium, provided the original work is properly cited.

DOI: 10.1002/aisy.202300702

R. Vonbank, C. Mucignat, I. Lunati  
Laboratory for Computational Engineering  
Empa - Swiss Federal Laboratories for Materials Science and Technology  
8600 Dübendorf, Switzerland

R. Katzschmann  
Soft Robotics Lab  
ETHZ - Swiss Federal Institute of Technology, ETH Zürich  
8092 Zürich, Switzerland

S. F. Armanini  
eAviation  
Department of Aerospace and Geodesy  
TUM School of Engineering and Design  
Technical University of Munich  
85521 Ottobrunn, Germany

Unmanned underwater vehicle (UUV) gliders are designed for long-range missions of up to one thousand kilometers.<sup>[1]</sup> The system requires energy only when inverting the vertical direction of motion, as a change in density is required. In order to save energy, the direction of vertical motion is changed as few times as possible. Consequently, UUVs are encouraged to sink as deep as possible before inverting. In principle, soft robotic actuation mechanisms withstand extreme pressures and thus can be regarded as pressure agnostic.<sup>[6]</sup> Moreover, due to their elasticity, such actuators have greater impact resilience.<sup>[7,8]</sup> These features ensure fewer repairs and maintenance to the wings; essential qualities in cluttered deep-sea environments. Most of the present literature regards the use of soft robotic actuation for undulatory propulsion in marine applications,<sup>[9–16]</sup> whereas this work focuses on using soft wings to maximize efficiency in UUVs. Here, the design and manufacturing process of a wing constituted of a soft silicone actuator and a rigid leading edge are explored. The wing aims to showcase the potential of soft-robotic principles in the underwater glider sector.

## 2. Design and Manufacturing

The soft wing assembly consists of a single milled aluminium leading edge and connector that secures the soft section. An exploded view of the soft wing compartment is shown in Figure 1a.

### 2.1. Design

As shown in Figure 1c, the compliant wing structure features two symmetric actuation chambers, which allow upward and downward deflection. By increasing the volume of one chamber and decreasing the volume in the other, significant camber morphing is achieved. An exploded view of the UUV wing section as well as a trimetric view of the right semi-wing is given in Figure 1a,b. A relatively thick symmetric hydrofoil (NACA0016) was selected, to increase the lift-to-drag ratio and maximize the inner volume of the wing, ensuring space for the wing chambers.<sup>[17]</sup> Based on a nominal forward velocity  $\vec{V}$  of the chosen reference UUV (see Section S1 and Figure S2, Supporting Information) of  $0.25 \text{ m s}^{-1}$  and on preliminary studies, an angle of attack (AoA) of  $\alpha = 12^\circ$  maximizes the efficiency of the chosen wing profile.<sup>[18]</sup> Since wings are mounted with  $\alpha = 0^\circ$  with respect to the underwater

gliders' longitudinal axis, the AoA of the vehicle coincides with that of the soft wing. To increase the generated lift  $\vec{L}$ , and reduce the manufacturing complexity, an untapered wing design with no sweep, aspect ratio (AR) of 1.6, and chord length of 230 mm was chosen.<sup>[1,19]</sup>

The internal structure of the wing consists of two main inflatable chambers that are connected by silicone tubes to a pump and separated from each other by an inextensible layer of 0.75 mm perforated polyethylene terephthalate foil. Each actuation chamber consists of 13 channels 4 mm wide, which cover the whole half wing lengthways. They have a height between 13.2 mm, at the leading edge, and 4.6 mm at the trailing edge. The channels are spaced 4 mm apart, have an external wall thickness of 2.5 mm and are connected individually at their base with passageways running chordwise to enable uniform pressurization.

### 2.2. Actuation

The two chambers of each semi-wing are connected in a closed hydraulic cycle featuring a peristaltic pump (A 9QX, Boxer GmbH, Ottoburen, Germany).<sup>[20]</sup> The electric circuit of the wing is housed in the hull of the UUV, while the hydraulic circuit is mounted externally. The interface between the two circuits is a pump driven by a transmission shaft. A cutaway view of the internal structure and its connection to the pump is given in Figure 1c. The pump is connected to a stepper motor (NEMA 14, Simac Electronics GmbH, Neukirchen-Vluyn, Germany) using a torsional coupling and driven by a stepper driver (UIM243L02BT, Boxer GmbH, Ottoburen, Germany) with a maximum of 480 rpm.

### 2.3. Fabrication

The geometry and the manufacturing process, lost wax technique, were adapted from previous work.<sup>[21]</sup> Compared to a single molded actuator, this approach allows stronger bonding of the assembly, and more precise external dimensions. Furthermore, reducing the number of interfaces between soft materials, which otherwise need to be glued or fitted together, reduces the risk of failure under pressure. A manufacturing flow-chart is given in Figure 2.

The inextensible layer is laser cut and roughened using sandpaper to increase the bonding strength with the silicone. The outer shells are fused deposition modelling (FDM) printed using

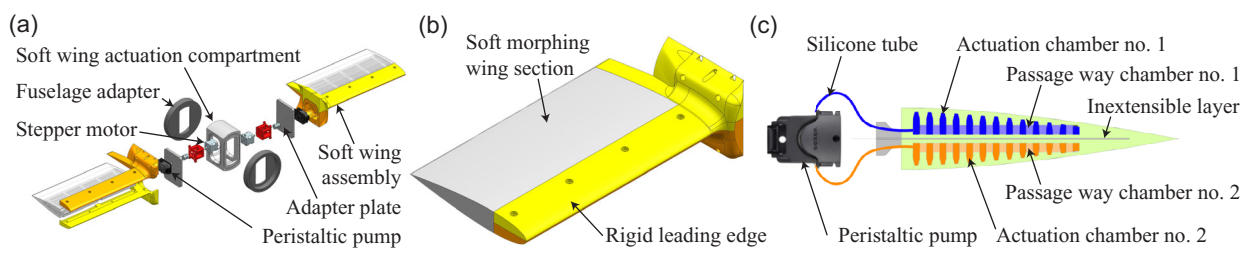


**Figure 1.** Overview of the soft robotic wing components. Scale bar corresponding to 100 mm. a) Exploded view of the soft wing actuation compartment showing the wing, the pressure hull adapter, and the peristaltic pumps. b) CAD rendering of the wings with rigid parts in yellow and the soft morphing section in gray. c) Cross-section of the wing and the pump (enlarged scale). The two chambers, in blue and orange, are connected through the peristaltic pump.

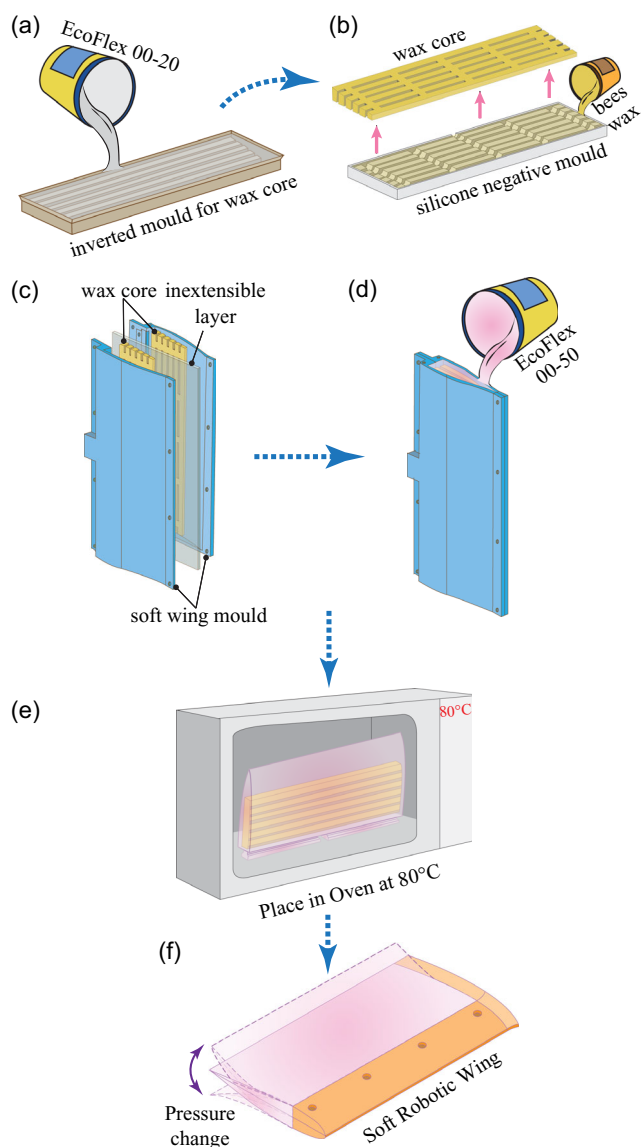


**Figure 2.** Manufacturing process of the soft, hydraulically actuated wing. a) Using a 3D-printed mold, an inverted silicone mold is cast using EcoFlex 00-20. b) The silicone negative mold is used to cast a bee wax core of the inner wing structure. c) Two wax cores (one for each actuation chamber) are assembled with the soft wing mold and an inextensible layer in between. d) EcoFlex 00-50 is poured into the fixed mold assembly. e) After curing the silicone, the mold is placed inside an oven at 80 °C to liquefy the wax cores. The molten wax flows out of the chambers and empty cavities are generated. f) The finished soft wing section is mounted to the stiff leading edge and is ready for assembly.

conventional PLA, coated with epoxy (XTC-3D, Smooth-On, Inc., Macungie, US) to decrease surface roughness, and then sprayed with mold release agent (Ease Release 200, Smooth-On, Inc., Macungie, US). For the wax pattern, a negative mold is designed and FDM printed. With this, a positive mold is cast using soft silicone (EcoFlex 00-20, Smooth-On, Inc., Macungie, US). The wax (beeswax pastilles, API LINE GmbH, Erlenbach, CH) is melted at 80 °C and poured into the silicone mold. After

solidification, the outer shells are assembled, and the two wax patterns are inserted inside. The inextensible layer is positioned between the two wax cores and all components are fixed in place using screws. To produce the wing, two-component addition-curing silicone (EcoFlex 00-50, Smooth-On, Inc., Macungie, US) is used. The processing time is extended during casting by adding a retarding additive (SLO-JO, Smooth-On, Inc., Macungie, US) and the liquid silicone is placed in a vacuum chamber at 40 Pa for 10 min. The liquid silicone is then poured into the prepared molds at a shallow angle and shaken to prevent air pockets. Finally, the mold is again placed in the vacuum chamber at 400 Pa for 10 min, to extract any air bubbles, and then left to cure overnight in ambient conditions. After curing, excess material is removed and the outer shells are carefully opened. To remove the wax, the wing is inserted upright in an oven at 80 °C and then rinsed in water. A silicone tube (Innovaprene P60, Boxer GmbH, Ottobereun, Germany) is bonded to each port to connect the chambers to the pump.

### 3. Experimental Section

Initial actuator tests were conducted in a stationary water tank to qualitatively assess the durability and deflection range of the manufactured wing section. Successively, experiments in a water flow channel were executed to investigate the morphing wing's performance under various flow conditions.

#### 3.1. Water Tank Characterization

To analyze the soft wing in stationary water conditions, the wing system was mounted inside a water tank, in a vertical configuration (leading edge pointing upwards and submerged to a depth of 30 mm from the water surface). This orientation of the wing minimizes buoyancy and gravity-related bending of the soft structure, permitting deflection caused only by the actuation of the silicone section. A camera was positioned parallel to the wing to capture the deflection of the trailing edge. A checkered sheet of plastic was placed behind the water tank to act as a fiducial marker. The volumes in the upper and lower chambers of the silicone section were controlled using the peristaltic pump setup described in Section 2. The deflection was measured visually by means of the camera setup. The 120 mL deflected state is shown in Figure S3, Supporting Information. Video S1, Supporting Information (Figure S7 in Section S2, Supporting Information) shows the inflation process from 0 to 120 mL, and back to the neutral position in stationary water conditions.

#### 3.2. Water Channel Characterization

To investigate the performance of the wing and determine its hydrodynamic coefficients, the soft robotic wing was tested in a large-scale water channel (3a) with a length of 6 m and a cross-section of  $0.6 \times 1$  (m<sup>2</sup>). The water bulk speed was in the range between 0.02 and 1.5 m s<sup>-1</sup> and controlled by a variable speed pump. The wing was positioned vertically at the beginning of the tunnel, and fixed in place by mechanical connectors. Its wingspan was in the direction of gravity and its chord lines (if  $\alpha = 0^\circ$ ) parallel to the tunnel's longitudinal axis. The origin of

the reference frame was positioned on the water surface at the leading edge of the wing. The  $x$ -axis was parallel to the longitudinal axis of the water channel, thus parallel to the flow velocity vector. The  $z$ -axis was oriented downwards parallel to gravity, while the  $y$ -axis formed a right-handed triad with the other two axes. The coordinate system is depicted in **Figure 3b**. To measure all external forces acting on the wing, a 6-axis load cell (FTN-GAMMA-IP68, Schunk GmbH & Co. KG, Mengen, Germany), capable of measuring a maximum force of 65 N and maximum torque of 5 Nm, was secured to the top side of the mechanical connectors. A rotation device was inserted below the load cell to adjust and measure the AoA without changing the orientation of the load cell. A cylindrical adapter was attached below the rotation device to pass the hydraulic tubes of the actuation system to the pump. To benchmark the performance of the proposed soft wing, a completely rigid wing featuring the same NACA0016 profile and dimensions was manufactured and tested. Each wing was submerged to a depth of 60 mm from its upper edge, so as to reduce the air/water boundary effects on the measurements, especially those proportional to the flow speed. **Figure 3b** illustrates the assembly immersed in water. This setup prevented additional drag on the wing, as it limited boundary-induced effects on the wing itself, lying deeper below the water surface. The load cell measured the resultant of all forces acting on the assembly on the three axes, namely gravity and fluid forces. Force measurements on the cylindrical adapter without a wing attached were performed for each flow speed, and the obtained lift and drag were subtracted from corresponding wing force measurements. Under these conditions, skin friction and wave drag were the dominant drag components acting on the assembly. Although this method does not account for 3D effects, such as the interaction between the wing and the connecting adapter, these are second order and negligible in this study. Given that the soft wing was approximately buoyancy neutral (EcoFlex specific gravity equal to 1.07), the sum of the forces

acting along the  $z$ -axis (i.e., gravity and buoyancy, which are constant in time) is zero. Hence, the  $z$  component of the forces resultant acting on the wing is not considered in the following analysis. **Figure 3b** shows the tested configuration, the assembly components as well as the reference frame. Additional information about the experimental setup is available in Section S2 and **Figure S4**, Supporting Information. Furthermore, a 3D virtual reconstruction of the wing was generated throughout all experiments. To achieve this, three cameras (c42, Raytrix GmbH, Kiel, Germany) were employed to capture the image of the wing, which had been painted with randomly placed black markers. The reconstruction process involved the recognition and triangulation of these markers, serving as reference points for the construction of an accurate 3D surface model of the wing. This enables the measurement of the actual chord length under deflection, required to calculate the drag and lift coefficients  $C_D$  and  $C_L$ , respectively. Further information concerning the 3D reconstruction can be found in Section 3. An example is given in **Figure 4**.

## 4. Results and Discussion

In the following sections, the results of the stationary water tests and water channel tests are summarized and discussed.

### 4.1. Water Tank Tests

The initial deflection test was conducted by inflating the actuation chambers to different volumes, while submerged in the stationary water tank. At all deflection states, the peristaltic pump is able to maintain the wing shape without power from the stepper motor.

As a result of the mechanical properties of the silicone, high wing deflection causes twisting along the span. At the maximum

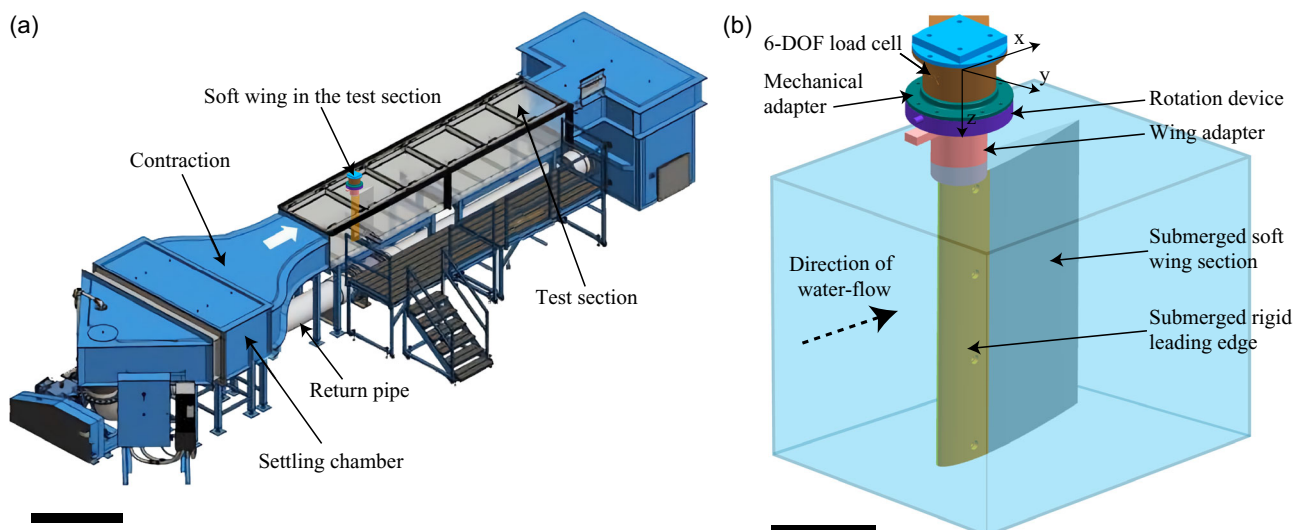


**Figure 3.** Overview of the tests performed in the water-flow channel. a) A rendering of the Empa/ETH Zürich large-scale water channel used for testing the soft wing. The same setup was used in ref. [26]. The scale bar corresponds to 2 m. b) Measurement setup illustrating the configuration in which the wing is positioned in the water channel. The setup consists of a 6-axis load cell, a rotating device, mechanical adapters, and the wing section. Scale bar corresponding to 100 mm.



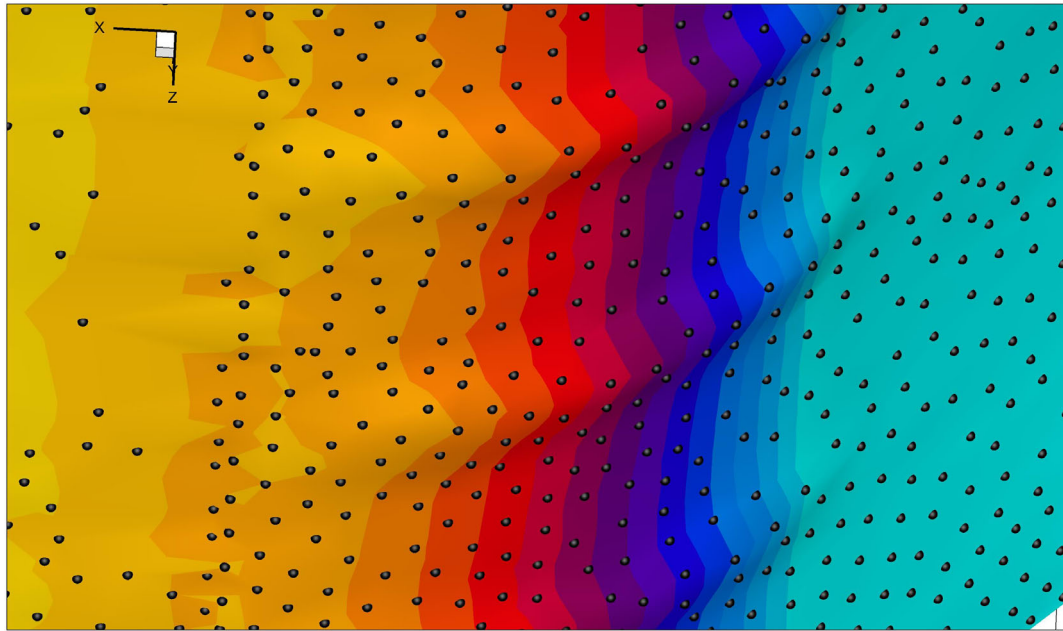


**Figure 4.** 3D scatter plot of the position of the markers superimposed to the reconstructed surface for a free-stream velocity of  $0.2 \text{ m s}^{-1}$  in negative x-direction,  $\text{AoA} = 12.5$  and inflation of 120 mL.

inflation level of 120 mL, the non-uniformity is most pronounced with a total variation of 5 mm at the trailing edge. In contrast, the rigidity of the outer walls led to slight deflections at both wingtips.

#### 4.2. Water Channel Tests

To characterize the hydrodynamic coefficients of the wing, a selection of  $\text{Re}$  numbers,  $\text{AoA}$ , and inflation levels were tested. The investigated flow speeds and testing conditions are summarized in **Table 1**. The  $\text{Re}$  number was calculated based on a water density  $\rho = 998 \text{ kg m}^{-3}$ , a water dynamic viscosity  $\mu = 0.001 \text{ Pa s}$ , and a chord length  $c = 0.23 \text{ m}$  for the undeflected wing. The fluid properties refer to the ambient temperature  $T_a = 20^\circ \text{C}$ . Experiments were performed with wing dimensions corresponding to those of typical underwater gliders in use. However, UUVs might require wings of different dimensions,

in which case correction factors will have to be applied to the below results to ensure coherence with the involved phenomena.

Since  $\text{Re}$  does not exceed  $10^5$ , the flow is expected to be mainly laminar, with flow separation occurring at high angles of attack.<sup>[22]</sup> For each of the above  $\text{Re}$ , five wing deformations were tested, referred to as “inflation levels”, the difference in volume between the two chambers, in milliliters (mL). Inflation is directly proportional to deformation. The inflation levels tested in the experiments are neutral, 30, 60, 90, and 120 mL, where neutral means equal inflation in both chambers, leading to symmetric airfoil and no wing deformation. At the flow speed of interest of  $0.25 \text{ m s}^{-1}$ , intermediate inflation levels of 15 and 45 mL were also studied. Also, for the same flow speed, all inflation values were tested in both directions, bringing about a positive and negative y-axis deflection. A 3D reconstruction of the soft wing’s surface was performed for all measurements. As mentioned above, the reconstructed wing was used to determine the chord length of the deflected wing profiles for further calculations. A 2D plot of the reconstructed wing is shown in **Figure 5**.

In contrast, the transient phase, occurring while the wing’s deformation is being altered, was not included in this study. The pump employed less than 60 s to displace water between the two chambers. After each deformation, while no measurements were taken, the system was given 60 s to reach equilibrium. When switching to a different deformation, the wing was first brought to the neutral (non-deformed) state and, after 60 s, to the target deformation. This procedure minimized the effects of the transient phase on the measurements taken during the experimental campaign. The wing’s transient phase has a negligible effect on the dynamics of UUVs, given that it takes place for a few meters in an overall mission range<sup>[23]</sup> of thousands of kilometers. Finally, the rigid wing was also tested in

**Table 1.** Investigated water channel flow speeds, corresponding  $\text{Re}$  numbers, and tested  $\text{AoAs}$  and inflation states.

| Flow speed<br>[ $\text{m s}^{-1}$ ] | $\text{Re}$ number<br>[ $e + 04$ ] | $\text{AoAs}$ [ $^\circ$ ]  | Inflation states [mL]  |
|-------------------------------------|------------------------------------|-----------------------------|--|
| 0.15                                | 3.44                               | −5; 0; 5; 7.5; 10; 12.5; 15 | neutral; 30; 60; 90; 120   |
| 0.20                                | 4.59                               | −5; 0; 5; 7.5; 10; 12.5; 15 | neutral; 30; 60; 90; 120   |
| 0.25                                | 5.74                               | −5; 0; 5; 7.5; 10; 12.5; 15 | neutral; $\pm 15 \pm 30$ ; $\pm 45$ ;<br>$\pm 60$ ; $\pm 90$ ; $\pm 120$ |
| 0.30                                | 6.89                               | −5; 0; 5; 7.5; 10; 12.5; 15 | neutral; 30; 60; 90; 120   |
| 0.40                                | 9.18                               | −5; 0; 5; 7.5; 10; 12.5; 15 | neutral; 30; 60; 90; 120   |

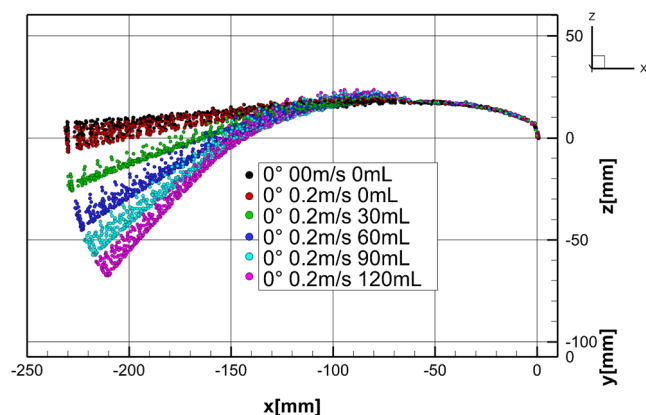


**Figure 5.** Bottom-view of the wing indicating the detected markers at the five investigated inflations and an AoA of  $0^\circ$  at  $0.2 \text{ m s}^{-1}$  free-stream velocity. For reference, the 0 mL inflation at no water flow is given in black.

all described AoAs and velocities. Regarding the force measurements, for each experiment, the averages of 1000 force readings were employed to calculate the lift and drag coefficients, hereafter indicated as  $C_L$  and  $C_D$ , and defined as follows:

$$C_L = \frac{|\vec{L}|}{\frac{1}{2} \rho \vec{V}^2 S} \quad (1)$$

$$C_D = \frac{|\vec{D}|}{\frac{1}{2} \rho \vec{V}^2 S} \quad (2)$$

Note that in Equation (1) and (2) the denominator consists of the product of the kinetic energy per unit volume ( $\frac{1}{2} \rho \vec{V}^2$ ) and the wing's reference area  $S$  projected on the  $xz$ -axis. Furthermore, we also computed the ratio of  $C_L/C_D$ , which is an indicator of the wing's efficiency. Since the drag readings are often close to zero, in this latter case we made use of the median of 1000 force readings, ensuring a more reliable result. For the sake of conciseness, the lift-to-drag ratio plots for all tested conditions are reported in Section S4, Figure S7 and S8, Supporting Information. **Figure 6** shows lift and drag measured at an inflation of 30 mL, for the different flow speeds. Lift and drag increase

with AoA up to a value of  $12.5^\circ$ ; thereafter, there is a fall in lift and a sharp rise in drag. This finding is in agreement with the predicted behaviour of the employed wing profile.

While the UUV's nominal forward velocity is  $0.25 \text{ m s}^{-1}$ , the  $C_L$ ,  $C_D$ , and  $C_L/C_D$  plots show the behavior of the soft robotic wing at the velocities given in Table 1. At all Re numbers,  $C_D$  and  $C_L$  increase with the AoA. At any AoA, with the exception of stalling conditions, higher inflation leads to greater lift and drag. These stalling conditions appear at a lower AoA when inflation is higher. Moreover, at the lowest flow speeds (**Figure 7** and **8**), this is particularly pronounced for steeper AoAs, where a sharp decrease in  $C_L$  and an increase in  $dC_D/d(\alpha)$  are witnessed. This is due to flow separation, resulting in less lift and additional drag (wake resistance). This is not the case for the neutral state, the rigid wing, or the least inflated wing configurations, which now feature higher lift than the more inflated conditions. Specifically, in **Figure 8**, at  $\alpha = 12.5^\circ$ , the 60 mL curve features a higher lift than the 90- and 120- mL curves. Additionally, the 90- mL inflation  $C_L$  curve plunges below the 30- mL curve. Increasing the inflation of the soft wing modifies the hydrofoil profile, augmenting its deformation and camber. Increasing the flow speed to  $0.4 \text{ m s}^{-1}$  (**Figure 11**) allows even the 120 mL configuration to delay stall to  $\alpha = 15^\circ$ . This is due to the higher pressure developed at faster flow speeds, which increases the ability of the flow to stay attached to convex surfaces. The effect of increased camber on  $C_L$  and  $C_D$  of morphing wings is also found in literature.<sup>[24]</sup>

Comparing the neutrally inflated soft wing with its rigid counterpart, the effects of surface refinement and structural stiffness are evident. At a flow speed of  $0.25 \text{ m s}^{-1}$  and  $\alpha = 15^\circ$  (**Figure 9**), the soft wing shows a sharp increase in drag and a drop in lift, whereas the rigid wing's hydrodynamic coefficients maintain their rising trend, and no significant changes in  $dC_D/d(\alpha)$  or  $dC_L/d(\alpha)$  are observed. After applying a Fourier transform and analyzing corresponding distributions in the frequency space, both rigid and soft wing show intensity peaks at 11 and 16 Hz. The soft wing also features an intensity peak at 3 Hz. The common peaks represent oscillations attributable to the system (vibrations and sensor noise), whereas the 3 Hz frequency intensity peak is likely due to fluttering of the soft wing. This phenomenon, together with the slight stalling behavior present

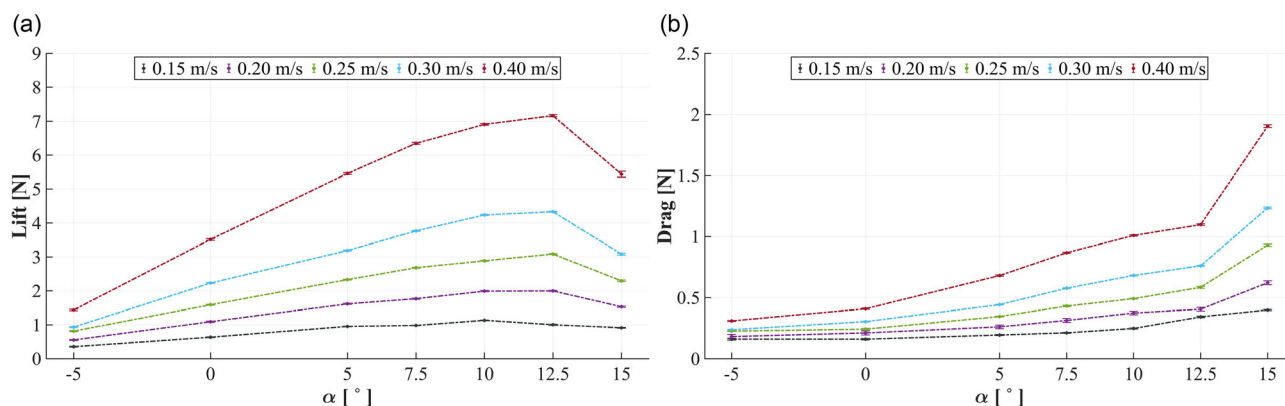


**Figure 6.** Measured fluid forces on soft wing with 30 mL inflation, for different flow speeds. a) Lift against AoA. b) Drag against AoA. All error bars represent the 95% confidence interval, calculated using a z score equal to 1.96.

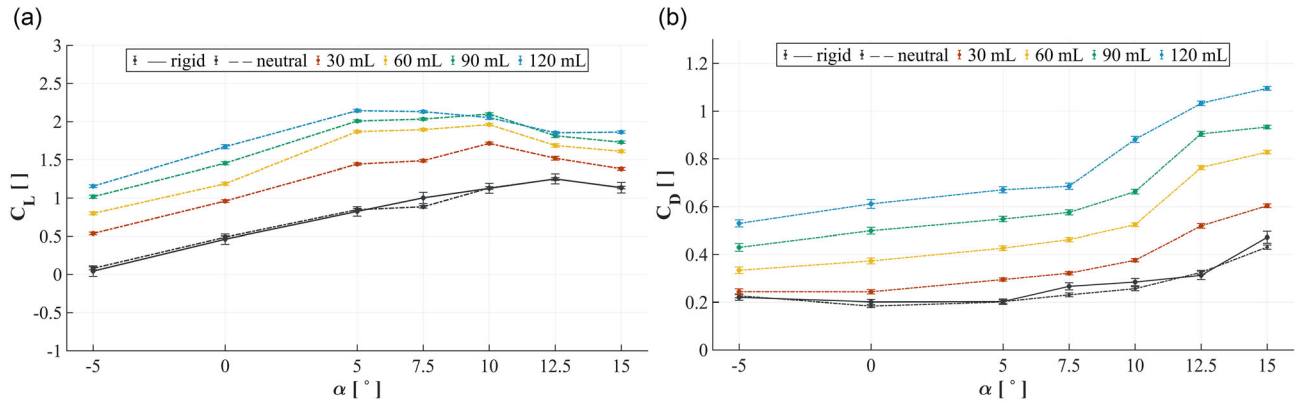


**Figure 7.** Measured coefficients at flow speed  $\nu = 0.15 \text{ m s}^{-1}$  ( $\text{Re} = 3.44e + 04$ ). a)  $C_L$  against AoA. b)  $C_D$  against AoA. All error bars represent the 95% confidence interval, calculated using a z score equal to 1.96.

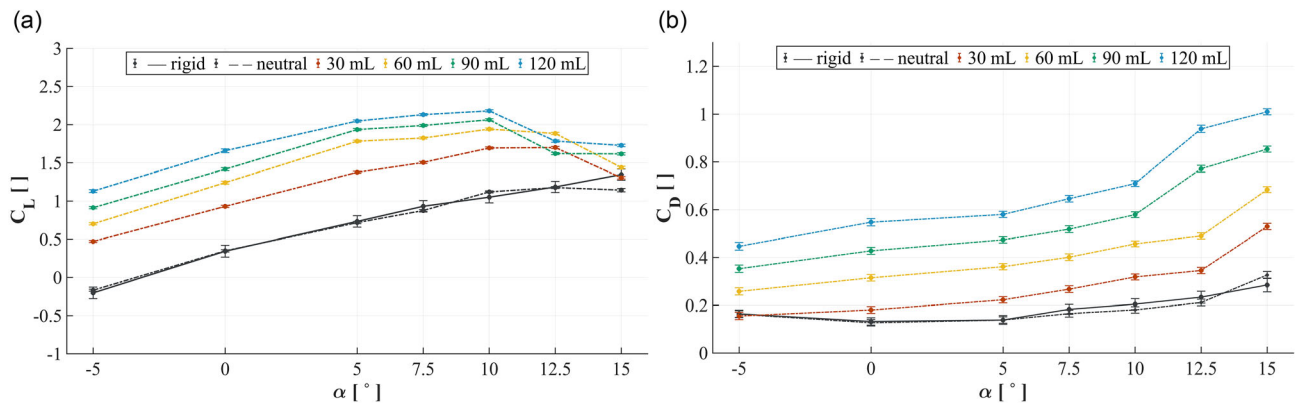


**Figure 8.** Measured coefficients at flow speed  $\nu = 0.2 \text{ m s}^{-1}$  ( $\text{Re} = 4.59e + 04$ ). a)  $C_L$  against AoA. b)  $C_D$  against AoA. All error bars represent the 95% confidence interval, calculated using a z score equal to 1.96.

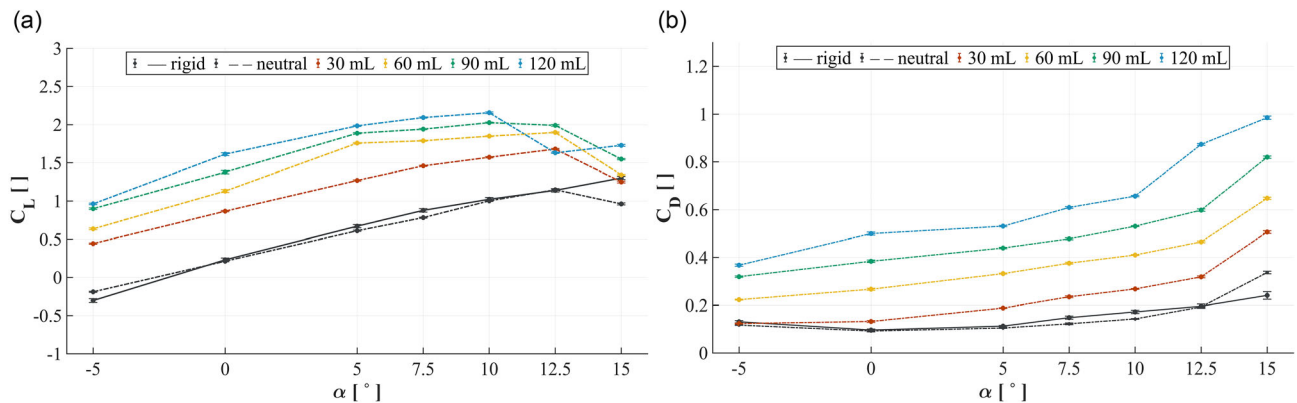


**Figure 9.** Measured coefficients at flow speed  $\nu = 0.25 \text{ m s}^{-1}$  ( $\text{Re} = 5.74e + 04$ ). a)  $C_L$  against AoA. b)  $C_D$  against AoA. All error bars represent the 95% confidence interval, calculated using a z score equal to 1.96.

in Figure 8 and 10, explains the divergence of  $C_L$  and  $C_D$  between the rigid and soft wing in its neutral position. This is especially evident at higher flow speeds and AoAs for which stalling and flutter intensify.<sup>[25]</sup> Also, the lower stiffness of the soft wing works as a damper to the mechanical system as a whole and

is likely to be the reason behind smaller confidence intervals in soft wing curves. Finally, in Figure 7–11, the  $C_L$  curve relative to symmetric hydrofoils (referred to as neutral and rigid) never intersects the origin. This is probably due to slight AoA misalignment during the experiment campaign, as, for obvious

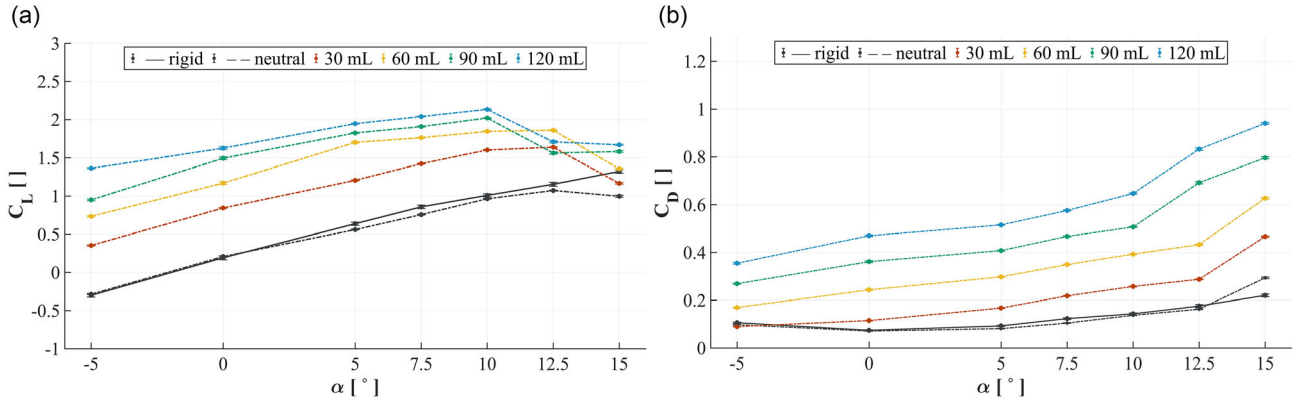


**Figure 10.** Measured coefficients at flow speed  $\nu = 0.30 \text{ m s}^{-1}$  ( $\text{Re} = 6.89e + 04$ ). a)  $C_L$  against AoA, for representative AoA and inflation levels. b)  $C_D$  against AoA, for representative AoA and inflation levels. All error bars represent the 95% confidence interval, calculated using a z score equal to 1.96.

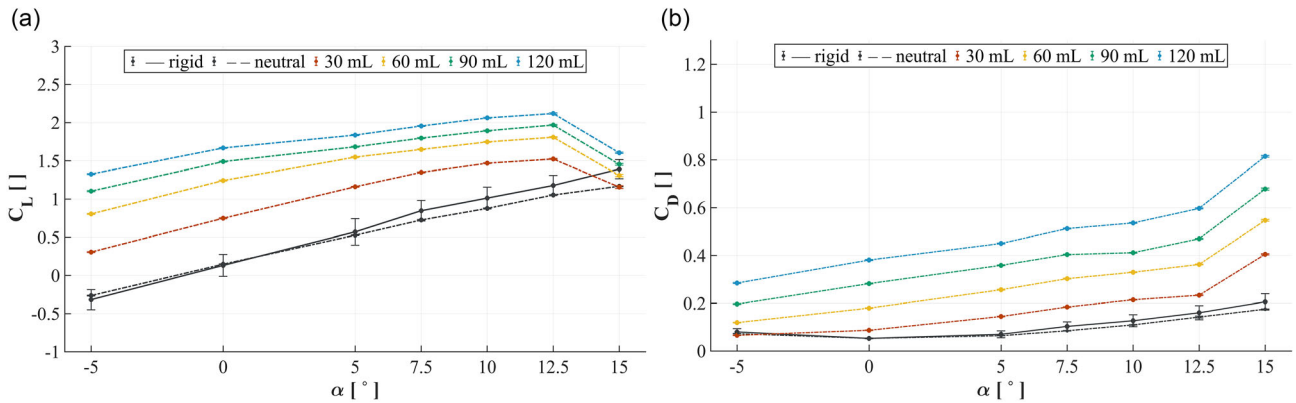


**Figure 11.** Measured coefficients at flow speed  $\nu = 0.40 \text{ m s}^{-1}$  ( $\text{Re} = 9.18e + 04$ ). a)  $C_L$  against AoA, for representative AoA and inflation levels. b)  $C_D$  against AoA, for representative AoA and inflation levels. All error bars represent the 95% confidence interval, calculated using a z score equal to 1.96.

geometrical reasons, the lift of a symmetric hydrofoil measured at  $\alpha = 0^\circ$  should be zero.

The capability of the soft wing to extend the maneuverability of the UUV is clear in **Figure 12**. Here, the left panel shows the scatter plot of  $C_L/C_D$  for rigid and soft wing at a flow speed of  $0.25 \text{ m s}^{-1}$  and inflation levels between  $-120$  and  $+120 \text{ mL}$ . On the right panel, the color-map illustrates the achievable  $C_L/C_D$  ratio for any given combination of  $\alpha$  and inflation level. The plot shows that the soft wing can generate much higher  $C_L/C_D$  for positive inflation levels until approaching stalling conditions, or negative lift at small AoA and negative inflation. Note that at the operational AoA of  $12.5^\circ$ , the lift-to-drag ratio can be increased by 10% or decreased by 70% compared to the rigid wing. Moreover, at an AoA of  $5^\circ$ , the value of  $C_L/C_D$  varies from  $-2$  to about  $7$  for the soft wing (here the rigid one operates at a fixed value of  $6$ ), thus offering a competitive advantage with respect to traditional fixed wings. This comparison can be extended to UUVs. While a traditional rigid-wing UUV needs to modify its AoA in order to generate sufficient lift, a soft-wing UUV can achieve comparable lift simply by modifying its inflation level. The only other lift-related difference is that generated

by the fuselage and other surfaces of the vehicle, which the former brings to a higher AoA and thus higher lift. However, this difference is negligible and can be balanced by an additional inflation of the soft wing. Furthermore, in rigid-wing UUVs, the increased inclination of the fuselage raises both fuselage and wing drag, as expressed in Equation (3) (where  $\alpha$  is the AoA and  $\alpha_0$  is a generic AoA). In soft-wing UUVs instead, lift generation causes an increase in wing drag only. A comparison between the drag of the two UUV configurations can be extracted from Equation (4), a Taylor expansion of the vehicle's drag around the generic gliding angle  $\alpha_0$ . Here, the total drag  $D_{\text{tot}}$  acting on the vehicle equals the sum of fuselage drag  $D_F$  and wing drag  $D_W$ . Due to the lift generation method described above, the term  $(\alpha - \alpha_0)$  is smaller for soft-wing UUVs, hence providing equal lift with a smaller increase in drag with respect to rigid-wing UUVs. For the same velocity  $\vec{V}$ , the difference in AoA for UUVs featuring rigid (13 a) and soft wings (13 b) is illustrated in **Figure 13**.

$$D_{\text{tot}}(\alpha_0) = D_F(\alpha_0) + D_W(\alpha_0) \quad (3)$$



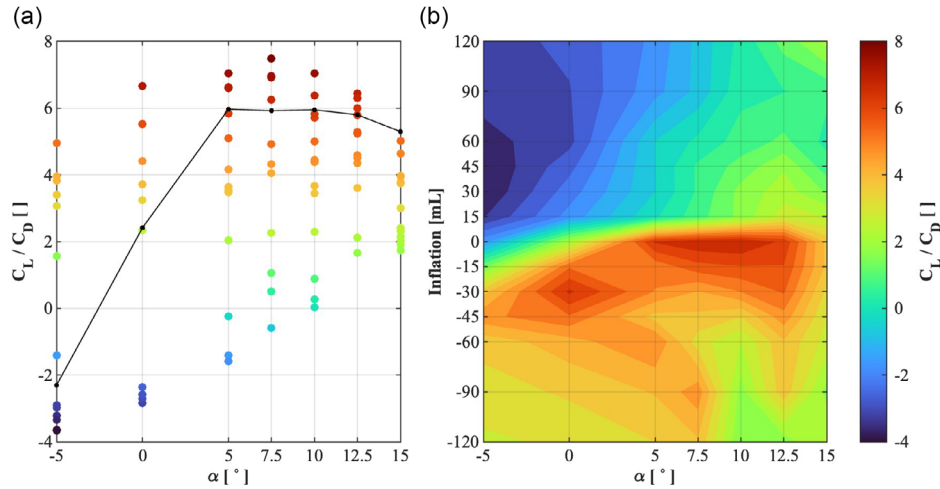


**Figure 12.** At flow speed of  $0.25 \text{ m s}^{-1}$  (vehicle's operational speed,  $\text{Re} = 5.74e + 04$ ), a) efficiency ( $C_L$  to  $C_D$  ratio) at every inflation level for the soft wing (scattered dots) and rigid wing (solid black curve). Scattered dots are coloured according to the colorbar legend on the right hand side. b) Colormap of the soft wing efficiency ( $C_L$  to  $C_D$  ratio), with colorbar legend to the right-hand side.

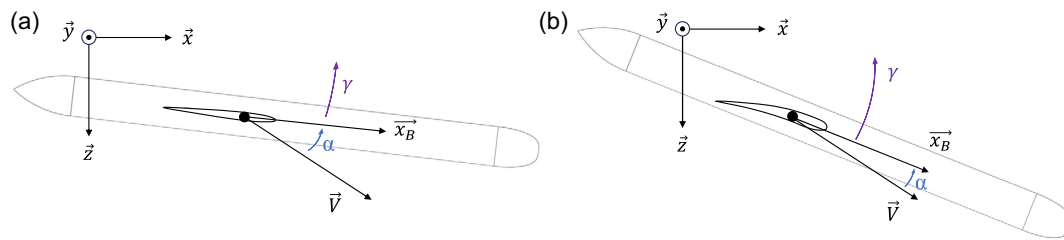


**Figure 13.** Comparison of two UUVs with velocity vector  $\vec{V}$ , body axis  $\vec{x}_B$ , pitch angle  $\gamma$  and featuring rigid and soft wings. a) Rigid wing-equipped UUV at a large AoA. b) Soft wing-equipped UUV at a modest AoA. Configuration b generates lower fuselage drag and equal lift, allowing for a reduced total cost of transport of the UUV.

$$D_{\text{tot}}(\alpha) \sim D_F(\alpha_0) + \frac{d(D_F(\alpha_0))}{d\alpha}(\alpha - \alpha_0) + D_W(\alpha_0) + \frac{d(D_W(\alpha_0))}{d\alpha}(\alpha - \alpha_0) \quad (4)$$

## 5. Conclusion

A soft robotic morphing wing for an underwater glider was designed, manufactured, and tested successfully. The pressure-proof soft wing features a symmetric NACA0016 profile, consisting of a rigid leading edge and a soft silicone actuator manufactured using lost-wax core molding. To actuate and control the wing's deflection, the silicone assembly has two non-communicating chambers inflated by a peristaltic pump. Stationary water tank tests and water channel tests were performed to monitor its morphing behavior and characterize the wing's hydrodynamic performance. During water channel tests, force data were acquired at five Reynolds numbers, seven AoAs, and a minimum of five different soft wing inflation levels. Generally, increasing the AoA results in an increment in both fluid forces and hydrodynamic coefficients. Also, higher inflation

states cause a shift to lower AoA of general behaviour and stalling points. Exploiting different inflation states, the present soft wing achieves bi-directional deflection, crucial to the vehicle's vertical motion. Compared to a traditional rigid wing, at the operational AoA of 12.5, the lift-to-drag ratio of the soft wing ranges from  $-70\%$  to  $+10\%$  and depends on its inflation state. This article lays the groundwork for future research towards the implementation of soft robotics on underwater gliding vehicles. Indeed, when implemented on UUVs, the soft wing supplies the required lift without needing to change the AoA of the vehicles or increasing the total drag. Therefore, the soft wing reduces the total cost of transport of the UUVs on which it is implemented.

## Supporting Information

Supporting Information is available from the Wiley Online Library or from the author.

## Acknowledgements

A.G., L.A., D.L., and F.W. contributed equally to this work. We would like to thank the other members of the Aerial Robotics Lab, Imperial College London, and Sustainability Robotics Laboratory, Empa, for their support

and numerous stimulating discussions on this topic. Furthermore, we would like to thank the whole Nautilus team for their work on the design of the UUV, Ardian Jusufi for providing advice on the design of the structure, and Felix Dannert and Marco Trentini for envisioning this project in collaboration with ARIS. This work was partially funded by EPSRC (award no. EP/R00953/1 (CASCADE), and EP/R026173/1 (ORCA)), the EU H2020 AeroTwin project (grant ID 810321), Royal Society Wolfson fellowship (RSWF/R1/180003), NERC (award no. NE/R012229/1), the UKAEA, and the Empa-Imperial research partnership.

## Conflict of Interest

The authors declare no conflict of interest.

## Data Availability Statement

The data that support the findings of this study are available from the corresponding author upon reasonable request.

## Keywords

hydraulic actuation, hydrofoil, morphing wing, soft actuator, soft robotics, underwater glider, unmanned underwater vehicle

Received: October 27, 2023

Revised: January 2, 2024

Published online:

- [1] M. Y. Javaid, M. Ovinis, F. B. Hashim, A. Maimun, Y. M. Ahmed, B. Ullah, *Int. J. Nav. Archit. Ocean Eng.* **2017**, 9, 382.
- [2] M. R. Dhanak, N. I. Xiros, *Springer Handbook of Ocean Engineering*, Springer, Berlin, Germany **2016**.
- [3] Y. Singh, S. K. Bhattacharyya, V. G. Idichandy, *J. Ocean Eng. Sci.* **2017**, 2, 90.
- [4] M. A. Fatiha, B. Augier, F. Deniset, P. Casari, J. A. Astolfi, *J. Mar. Sci. Eng.* **2019**, 7, 12.
- [5] S. Barbarino, O. Bilgen, R. M. Ajaj, M. I. Friswell, D. J. Inman, *J. Intell. Mater. Syst. Struct.* **2011**, 22, 823.
- [6] R. K. Katzschmann, A. D. Marchese, D. Rus, *Springer Tracts in Advanced Robotics*, Vol. 109, Springer Verlag, Berlin, Germany **2016**, pp. 405–420.
- [7] G. Li, X. Chen, F. Zhou, Y. Liang, Y. Xiao, X. Cao, Z. Zhang, M. Zhang, B. Wu, S. Yin, Y. Xu, H. Fan, Z. Chen, W. Song, W. Yang, B. Pan, J. Hou, W. Zou, S. He, X. Yang, G. Mao, Z. Jia, H. Zhou, T. Li, S. Qu, Z. Xu, Z. Huang, Y. Luo, T. Xie, J. Gu, et al., *Nature* **2021**, 591, 66.
- [8] K. C. Galloway, K. P. Becker, B. Phillips, J. Kirby, S. Licht, D. Tchernov, R. J. Wood, D. F. Gruber, *Soft Rob.* **2016**, 3, 23.
- [9] B. Wang, Y. Chen, Y. Wu, Y. Lin, S. Peng, X. Liu, S. Wu, S. Liu, J. Yi, P. Polygerinos, Z. Wang, *Machines* **2022**, 10, 381.
- [10] R. K. Katzschmann, J. DelPreto, R. MacCurdy, D. Rus, *Sci. Rob.* **2018**, 3, eaar3449.
- [11] A. Maleeq, E. Palafox, S. AlSahhaf, L. Lickteig, S. Kang, T. DeAgostino, D. Choi, A. Alghafli, Seahawk: Biomimetic Shape Deposition Manufacturing (SDM) Fin Propulsion Assisted Sea Glider, <https://softroboticstoolkit.com/seahawk-sdm-glider> (accessed: March 2024).
- [12] L. Micklem, G. Weymouth, B. Thornton, in *2022 IEEE/RSJ Int. Conf. Intelligent Robots and Systems (IROS)*, IEEE, Piscataway, NJ **2022**, pp. 5464–5469.
- [13] Y. Li, D. Pan, Q. Zhao, Z. Ma, X. Wang, *Ocean Eng.* **2018**, 163, 51.
- [14] Y.-H. Lin, R. Siddall, F. Schwab, T. Fukushima, H. Banerjee, Y. Baek, D. Vogt, Y.-L. Park, A. Jusufi, *Adv. Intell. Syst.* **2023**, 5, 2000244.
- [15] U. Gupta, L. Qin, Y. Wang, H. Godaba, J. Zhu, *Soft Robots Based on Dielectric Elastomer Actuators: A Review*, IOP Publishing Ltd, Bristol, UK **2019**.
- [16] M. Xia, H. Wang, Q. Yin, J. Shang, Z. Luo, Q. Zhu, *J. Bionic Eng.* **2023**, 20, 934.
- [17] Z. Wang, Y. Li, A. Wang, X. Wang, in *Proc. - 2015 Int. Conf. Control, Automation and Robotics, ICCAR 2015*, Institute of Electrical and Electronics Engineers Inc., Piscataway, NJ **2015**, pp. 74–77, ISBN 9781467375238.
- [18] L. M. Meyers, V. Msomi, *Materials Today: Proceedings*, Vol. 45, Elsevier Ltd., London, UK **2021**, pp. 5456–5461, ISSN 22147853.
- [19] K. Hanif Nordin, M. Ovinis, M. Yasar Javaid, *ARPN J. Eng. Appl. Sci.* **2017**, 12, 10.
- [20] R. K. Katzschmann, A. De Maille, D. L. Dorhout, D. Rus, in *IEEE Int. Conf. Intelligent Robots and Systems*, Vol. 2016-November, Institute of Electrical and Electronics Engineers Inc., Piscataway, NJ **2016**, pp. 3048–3055, ISBN 9781509037629, ISSN 21530866.
- [21] A. D. Marchese, R. K. Katzschmann, D. Rus, *Soft Rob.* **2015**, 2, 7.
- [22] J. Winslow, H. Otsuka, B. Govindarajan, I. Chopra, *J. Aircr.* **2018**, 55, 1050.
- [23] R. E. Davis, C. C. Eriksen, C. P. Jones, *The Technology and Applications of Autonomous Underwater Vehicles*, Taylor & Francis, London, UK **2002**, pp. 37–58.
- [24] Y. Yining, *J. Phys.: Conf. Ser.* **2020**, 1519, 012020.
- [25] M. P. Paidoussis, S. J. Price, E. De Langre, *Fluid-Structure Interactions: Cross-Flow-Induced Instabilities*, Cambridge University Press, Cambridge, UK **2010**.
- [26] F. Schwab, F. Wiesemüller, C. Mucignat, Y.-L. Park, I. Lunati, M. Kovac, A. Jusufi, *Front. Rob. AI* **2022**, 8, 791722.